Publisher: GSA
Journal: GEOL: Geology
DOI:10.1130/G39995.1

Multisourced metals enriched by magmatic-hydrothermal fluids in stratabound deposits of the Middle–Lower Yangtze River metallogenic belt, China

Yang Li[1,2,3*], David Selby[1,4], Xian-Hua Li[2], and Chris J. Ottley[1]

[1]*Department of Earth Sciences, Durham University, DH1 3LE Durham, UK*

[2]*State Key Laboratory of Lithospheric Evolution, Institute of Geology and Geophysics, Chinese Academy of Sciences, 10029 Beijing, China*

[3]*Department of Geology and Geophysics, Yale University, New Haven, Connecticut 06511, CT, USA*

[4]*State Key Laboratory of Geological Processes and Mineral Resources, School of Earth Resources, China University of Geosciences, Wuhan, 430074, Hubei, China*

*E-mail: yang.li@yale.edu; cugliyang@126.com

ABSTRACT

Stratabound deposits within Late Carboniferous carbonate units in the Middle-Lower Yangtze River metallogenic melt are important Cu producers in China. Hitherto, the genesis of these deposits has been debated, due to poor constraints regarding the timing and source of the mineralization. Proposed models include a Late Carboniferous seafloor exhalative formation (SEDEX), or an Early Cretaceous magmatic-hydrothermal origin. These models imply different metal sources (basinal *vs* magmatic fluid, respectively) and would require different exploration strategies. New pyrite Re–Os and

Publisher: GSA
Journal: GEOL: Geology
DOI:10.1130/G39995.1

trace element results from the representative Xinqiao deposit favor a Cretaceous magmatic-hydrothermal genesis over a SEDEX origin. The distinct initial $^{187}Os/^{188}Os$ compositions (Os*i*) of different pyrite types (colloform Os*i* = 1.4 and euhedral grains Os*i* = 0.7), coupled with the pyrite trace element abundance, indicate that the Os, and by inference other metals (e.g., Cu, Ag, Au), are sourced from a Cretaceous magmatic-hydrothermal system (Os*i* = 0.7) and Late Permian metalliferous black shales (Os*i* = 7.6 ± 3.8). In addition, the genesis of Au-bearing stockwork pyrite veins hosted by the Carboniferous sandstone is best explained by the leaching of existing mineralization (e.g., porphyry Au-Mo) by Early Cretaceous magmatic-hydrothermal fluids. This is implied by the lack of common Os, high Re abundances (0.6–3.7 ppm), and highly variable Re–Os model ages (379 and 173 Ma), which are positively correlated with Re and total abundances of Co, Ni, Ag, Au, Tl and Ba. This study highlights the importance of recycling multi-sourced metals (sedimentary and existing mineralization) in the formation of intrusion-related stratabound deposits. Furthermore, it demonstrates the importance of integrating information regarding the source and timing of deposit formation within a well-defined geological framework, which can yield information about the ore-forming process and help to guide mineral exploration.

INTRODUCTION

Intrusion-related stratabound deposits, together with porphyry, skarn, and epithermal deposits, are important end-members of porphyry copper systems that contribute significantly to the world's supply of Cu, Mo Au, and other metals (Sillitoe, 2010). The presence of non-magmatic fluids in porphyry copper systems, i.e., meteoric

Publisher: GSA
Journal: GEOL: Geology
DOI:10.1130/G39995.1

and metamorphic fluids, has been ubiquitously documented (D'Errico et al., 2012; Fekete et al., 2016; Li et al., 2017a), but the current consensus is that the metals are derived from magmatic-hydrothermal systems. However, the close spatial association between metalliferous sedimentary rocks and many intrusion-related stratabound deposits raises the possibility that, in addition to magmatic-hydrothermal systems, metal-bearing strata could be a complementary origin of metals.

The expansive distribution of intrusion-related stratabound deposits in the Middle–Lower Yangtze River metallogenic belt (Fig. 1A) offers an excellent opportunity to examine the sources of their metals. These deposits comprise predominantly massive ores of chalcopyrite and pyrite, with quartz-Au-bearing pyrite vein stockworks. A unique feature of these stratabound deposits is the ubiquitous presence of colloform pyrite (Gu et al., 2007), and their close spatial association with Early Cretaceous magmatic-porphyry-skarn systems (Fig. 1). Although extensively studied, the genesis of these stratabound deposits remains ambiguous, with two principal genetic models having been proposed: 1) linkage to Early Cretaceous porphyry-skarn systems (Pan and Dong, 1999; Mao et al., 2011; Pirajno and Zhou, 2015); and 2) initial formation as a Late Carboniferous SEDEX system, which was then enriched/overprinted by an Early Cretaceous magmatic-hydrothermal event (Zeng et al., 2002; Gu et al., 2007). The contrasting genetic models imply different metal enrichment mechanisms and alternate mineral exploration programs. For example, an Early Cretaceous magmatic-hydrothermal origin suggests that these deposits are similar to manto-type deposits (Mao et al., 2011; Li et al., 2017b; Zhang et al., 2017) in Mexico and Chile (Meinert, 1982; Sato, 1984). Therefore, a magmatic origin of metals is most likely, with stratabound deposits being expected to

Publisher: GSA
Journal: GEOL: Geology
DOI:10.1130/G39995.1

center around Cretaceous granites. On the other hand, a Carboniferous SEDEX origin (Xu and Zhou, 2001; Zeng et al., 2002; Gu et al., 2007; Guo et al., 2011; Xie et al., 2014) would suggest that the metals were sourced from the underlying strata by a migrating basinal fluid, and therefore the stratabound mineralization could be more laterally extensive within the Late Carboniferous limestone.

Uncertainty regarding ore genesis in the Middle–Lower Yangtze River metallogenic belt is primarily due to the lack of constraint on the timing of mineralization and a poor understanding of the source of the metals, which is a typical challenge for hydrothermal deposit studies. Here, based on a robust geological framework, the representative Xinqiao deposit of the Middle–Lower Yangtze River metallogenic belt is selected for a pyrite Re–Os and trace element study, in order to provide an improved genetic understanding and yield implications for mineral exploration.

STRATABOUND DEPOSITS OF THE MIDDLE–LOWER YANGTZE RIVER METALLOGENIC BELT

As represented by Xinqiao, stratabound ore bodies in the Middle–-Lower Yangtze River metallogenic belt are hosted primarily by limestone and dolomite units within the Late–Middle Carboniferous Chuanshan–Huanglong formations. These units lie above the Early Carboniferous Gaolishan Formation sandstone (Figs. 1B and 1C). Minor massive pyritic ores are also present in overlying Permian and Triassic carbonate units. The deposits exhibit a close spatial association with Early Cretaceous (ca. 135−145 Ma) granitoids (Zhou et al., 2008; Li et al., 2010), which are hosted by Carboniferous–Permian carbonate units. Many of the granitoids are associated with porphyry and skarn mineralization (Mao et al., 2011; Pirajno and Zhou, 2015). The stratabound ore bodies

Publisher: GSA
Journal: GEOL: Geology
DOI:10.1130/G39995.1

predominantly comprise Cu-bearing pyrite and pyrrhotite (Li et al., 2017b). Unique to these deposits is pyrite exhibiting a colloform texture (Xie et al., 2014). In most cases, no direct contact relationship is observed between the colloform ore and sedimentary rocks, but veins bearing colloform pyrite are observed to locally cross-cut the Permian limestone (Fig. DR3). Vertical to sub-vertical Au-bearing pyrite stockworks occur beneath the stratabound ore bodies hosted by the Early Carboniferous Gaolishan Formation sandstone (Guo et al., 2011; Zhang et al., 2017).

PYRITE RE–OS AND TRACE ELEMENT RESULTS

Four styles of pyritic mineralization (Figs. 1 and 2) from Xinqiao were examined for Re–Os and trace element analysis. Deposit geology, sample details, analytical methods, and pyrite Re–Os and trace element data are presented in the GSA data repository. Euhedral pyrite grains (py1) from the stratabound ore body have Re and ^{192}Os concentrations of 1.5–3.6 ppb and 1.7–4.0 ppt, respectively, and yield a Re–Os isochron age of 135.5 ± 4.0 Ma (initial ^{187}Os/^{188}Os composition (Os*i*) = 0.79 ± 0.11; n = 5; MSWD = 2.2; Fig. 2E). Colloform pyrite (py2) from the stratabound ore body possesses 1.2–9.3 ppb Re and 2.0–43.4 ppt ^{192}Os, and yields a Re–Os isochron age of 136.6 ± 4.6 Ma (Os*i* = 1.35 ± 0.06; n = 11; MSWD = 5.4; Fig. 2E). Euhedral garnet-skarn pyrite (py3) contains 1.4–1.6 ppb Re and 1.4–2.1 ppt ^{192}Os. For py3, although only two samples (XQ15-5-3 and XQ15-5-4) were analyzed, which is not sufficient to yield a statistically valid isochron, the Re–Os data yield an errorchron with a date of 143 ± 16 Ma and an Os*i* of 0.63 ± 0.44 (Fig. 2E). The sandstone-hosted pyrites (py4) possess 57–3692 ppb Re, 1.3–43.1 ppt ^{192}Os, and negligible common Os (< 0.45%, Table DR1). The model ^{187}Re–^{187}Os ages of these pyrite grains range from 173.2 ± 1.7–359.0 ± 1.8 Ma (Fig. 2F).

Publisher: GSA
Journal: GEOL: Geology
DOI:10.1130/G39995.1

Overall, Py1 and Py3 are characterized by low trace element abundance, but contain moderate Mn, Cu, Pb, Zn, W, and Ag (Table DR2). Py2 has higher abundances of Mn, Sb, Cu, Pb, Zn and Ag; py4 enriched in Au, Ba, Co, Ni and Tl (Fig. 3A). For py4, a positive correlation is observed between the total abundances of Co, Ni, Ag, Au, Tl, Ba, Re and Re–Os model ages (Fig. 3B).

DISCUSSION AND IMPLICATIONS

Magmatic and Sedimentary Sourced Metals for Stratabound Ore

The Re–Os ages of py1 and py2 (135.5 ± 4.0 and 136.7 ± 4.6 Ma; Fig. 2E) suggest that the two types of mineralization (euhedral and colloform pyrite) were formed broadly contemporaneously, and are indistinguishable from the emplacement age of the Jitou Stock (138.5 ± 1.0 Ma; Li et al., 2017b) at Xinqiao. In addition, these ages overlap with the Re–Os age of the skarn pyrite, py3 (143 ± 16 Ma; Fig. 2E). Thus, a temporal link exists between the Early Cretaceous magmatic-skarn system associated with the Jitou Stock and the stratabound mineralization. This is inconsistent with a Carboniferous SEDEX origin (Xu and Zhou, 2001; Zeng et al., 2002; Xie et al., 2014).

At the time of emplacement of the Jitou Stock (138.5 ± 1.0 Ma), the skarn pyrite (py3) had an Os*i* of 0.74 ± 0.24. Taking this value as the maximum estimate of the magmatic Os*i*, a crust-derived origin with limited mantle input (Os*i* = 0.13) is inferred for the Jitou Stock. This is consistent with Jitou Stock zircon depleted Hf isotope composition (ε_{Hf} = ~– 11; Zhang et al., 2017). The similar Os*i* values (0.79 ± 0.11 *vs* 0.74 ± 0.24) for py1 and py3 imply that the Os, and by inference the associated metals, were predominantly sourced from the Early Cretaceous magmatic-hydrothermal system.

Publisher: GSA
Journal: GEOL: Geology
DOI:10.1130/G39995.1

It has been previously proposed that the colloform pyrite was initially formed in the Carboniferous (Xu and Zhou, 2001; Zeng et al., 2002; Gu et al., 2007; Xie et al., 2014), and then recrystallized to euhedral pyrite during the Early Cretaceous magmatic-hydrothermal event. This scenario is not supported by the sharp contact relationship between the euhedral and colloform pyrites (Fig. DR2A), nor by the cross-cutting relationship between the colloform pyrite and Permian limestones at Dongguashan and Wushan (Fig. DR3). In addition, the Os*i* (Fig. 2E) and trace element abundances (Figs. 3A and 3B) of py2 are distinct from py1, hence a recrystallization origin of py1 from py2 is unlikely. Further, the colloform pyrite is composed of fine-grained (80 nm–1.5 μm) cubic crystals and not framboids, which is inconsistent with a sedimentary origin (Sweeney and Kaplan, 1973). Moreover, *in-situ* sulfur isotope data for the four types of pyrite studied here have indistinguishable $\delta^{34}S$ values (0–4 ‰). All of these data support a magmatic-hydrothermal origin rather than a SEDEX genesis (Zhang et al., 2017).

The highly radiogenic Os*i* (1.35 ± 0.06) of the colloform pyrite indicates that the Os and by inference the metals are not solely magmatically derived. In the Xinqiao area, the most likely source to provide a radiogenic $^{187}Os/^{188}Os$ composition is the Late Permian metalliferous black shales. These shales are enriched in Re (403 – 1002 ppb) and Os (0.3 – 1 ppb) and yield an Early Cretaceous $^{187}Os/^{188}Os$ composition of 7.6 ± 3.8 (Yang et al., 2004). Therefore, the most geological plausible scenario is that the colloform pyrite was formed through intensive water-rock interaction between the Early Cretaceous magmatic-hydrothermal fluids and the Late Permian metalliferous black shales.

Cycling Existing Mineralization for the Au-Bearing Pyrite Stockworks

Publisher: GSA
Journal: GEOL: Geology
DOI:10.1130/G39995.1

The Au-bearing pyrite (py4) veins hosted by the sandstone underlying the stratabound ore body are dated at 138 ± 2.3 Ma (quartz fluid inclusion Rb–Sr; initial $^{87}Sr/^{86}Sr$ = 0.71138 ± 0.00014; Zhang et al., 2017), suggesting a temporal and genetic association with the Jitou Stock, which is further supported by fluid inclusion and $\delta^{18}O$ data from quartz co-precipitated with py4 (up to 597 °C and 63.7 % NaCl equiv.; 6.81 ± 2.76 ‰; Wang and Ni, 2009; Li et al., 2017b). In contrast, a 319 ± 13 Ma Re–Os age (n = 9; MSWD = 13; Guo et al., 2011) for py4 seems consistent with the hypothesis that these pyrite veins were the fluid conduit (stockwork feeder) for a Carboniferous SEDEX system (Xu and Zhou, 2001; Zeng et al., 2002; Gu et al., 2007). However, a SEDEX scenario is not supported by the following observations. First, py4 Re–Os data from both this study and Guo et al. (2011) share similar characteristics (enriched in Re and limited to no common Os) and yield highly variable model ages (173–379 Ma). Therefore, the py4 Re–Os data do not meet the necessary criterial for isochron dating. Second, py4 does not contain common Os, but in SEDEX systems, the basinal fluid must interact with the basement rocks, and hence should inherit common Os with a radiogenic Os*i* (Hnatyshin et al., 2015). Third, the pyrite veins beneath the stratabound ore body are structurally controlled and only possess silicified and sericite-bearing selvages (Wang and Ni, 2009; Guo et al., 2011; Li et al., 2017b). In contrast, the fluid conduits in SEDEX systems are developed in syn-sedimentary faults and are characterized by tourmaline- and albite-bearing alteration assemblages (Leach et al., 2005). As such, in accordance with the 138 ± 2.3 Ma Rb–Sr age (Zhang et al., 2017), we suggest that the sandstone-hosted mineralization was temporally associated with the Early Cretaceous magmatic-hydrothermal system.

Publisher: GSA
Journal: GEOL: Geology
DOI:10.1130/G39995.1

For py4, in order to yield geologically reasonable ages (ca 138 Ma), each sample has to be corrected using widely different and geologically implausible Os*i* (e.g., –223–59; Table DR1). Given the fact that these samples possess very high abundances of Re and radiogenic Os with negligible common Os, it is unlikely that the observed ages are caused by disturbance of the Re–Os systematics. In this regard, the most plausible genesis for py4 is the leaching of rocks enriched in Re and radiogenic Os by the Early Cretaceous magmatic-hydrothermal fluid. A higher degree of water-rock interaction resulted in the inheritance of more Re, ^{187}Os and trace elements, which is consistent with the positive correlations between model ages of py4 and their Re and trace element concentrations (Figs. 2F, 3A and 3B). Rhenium and Os concentrations are typically very low in crustal rocks (0.20 and 0.03 ppb, respectively), but are known to be high in molybdenite (e.g., hundreds to thousands ppm for Re and ppm level for ^{187}Os) and to a lesser extent in other sulfides, such as chalcocite, chalcopyrite, bornite, and pyrite (Selby et al., 2009; Stein, 2014). As such, the most likely source for the elevated Re (ppm level), radiogenic Os (^{187}Os, ppb level), and negligible common Os in py4 is porphyry-style Au-Mo mineralization.

Implications for Ore Genesis and Metals Origin

In the Middle–Lower Yangtze River metallogenic belt, stratabound deposits are all spatially associated with the Early Cretaceous magmatic-porphyry-skarn systems (Fig. 1A), and the ore-forming fluids and alteration assemblages have a close magmatic affinity, but barely show characteristics of typical SEDEX systems (Pan and Dong, 1999; Mao et al., 2011). As such, an Early Cretaceous intrusion-related carbonate replacement origin is suggested, with the stratabound orebodies being spatially controlled by the

unconformity between the Early Carboniferous sandstone and Late Carboniferous carbonate units, and the Au-bearing stockworks being a product of recycled pre-existing porphyry-style mineralization by the Early Cretaceous magmatic-hydrothermal fluid (Fig. 4).

This study highlights that coupling absolute timing and source constraints for mineralization with a detailed geological framework can significantly advance our understanding of the ore-forming process of intrusion-related stratabound deposits, and underpin exploration models. Further, the recycling of metals from metalliferous sedimentary rocks (i.e., black shales) and pre-existing mineralization by magmatic-hydrothermal fluids could be an important mechanism for the formation of ore deposits.

ACKNOWLEDGMENTS

YL acknowledges a 2-month fellowship and a grant (SKL-K201706) from IGG-CAS, and extends his gratitude to Jian-Wei Li for his encouragement during this study. DS acknowledges the Total endowment fund and Dida scholarship (CUG Wuhan). We thank Zhen-Ting Jiang for assistance with SEM imaging, and Ann Bauer, Alan Rooney and Rachael Bullock for editorial comments, and extend our thanks to the editor and reviewers of Geology for their constructive and insightful comments.

REFERENCES CITED

D'Errico, M.E., Lackey, J.S., Surpless, B.E., Loewy, S.L., Wooden, J.L., Barnes, J.D., Strickland, A., and Valley, J.W., 2012, A detailed record of shallow hydrothermal fluid flow in the Sierra Nevada magmatic arc from low-$\delta^{18}O$ skarn garnets: Geology, v. 40, p. 763–766, https://doi.org/10.1130/G33008.1.

227 Fekete, S., Weis, P., Driesner, T., Bouvier, A.S., Baumgartner, L., and Heinrich, C.A.,
228 2016, Contrasting hydrological processes of meteoric water incursion during
229 magmatic-hydrothermal ore deposition: An oxygen isotope study by ion microprobe:
230 Earth and Planetary Science Letters, v. 451, p. 263–271,
231 https://doi.org/10.1016/j.epsl.2016.07.009.
232 Gu, L.X., Zaw, K., Hu, W.X., Zhang, K.J., Ni, P., He, J.X., Xu, Y.T., Lu, J.J., and Lin,
233 C.M., 2007, Distinctive features of Late Palaeozoic massive sulphide deposits in
234 South China: Ore Geology Reviews, v. 31, p. 107–138,
235 https://doi.org/10.1016/j.oregeorev.2005.01.002.
236 Guo, W.M., Lu, J.J., Jiang, S.Y., Zhang, R.Q., and Qi, L., 2011, Re-Os isotope dating of
237 pyrite from the footwall mineralization zone of the Xinqiao deposit, Tongling, Anhui
238 Province: Geochronological evidence for submarine exhalative sedimentation:
239 Chinese Science Bulletin, v. 56, p. 3860–3865, https://doi.org/10.1007/s11434-011-
240 4770-y.
241 Hnatyshin, D., Creaser, R.A., Wilkinson, J.J., and Gleeson, S.A., 2015, Re-Os dating of
242 pyrite confirms an early diagenetic onset and extended duration of mineralization in
243 the Irish Zn-Pb ore field: Geology, v. 43, p. 143–146,
244 https://doi.org/10.1130/G36296.1.
245 Leach, D., Sangster, D., Kelley, K., Large, R., Garven, G., Allen, C., Gutzmer, J., and
246 Walters, S.G., 2005, Sediment-hosted lead-zinc deposits: A global perspective:
247 Economic Geology and the Bulletin of the Society of Economic Geologists, v. 100,
248 p. 561–607.

Li, X.H., Li, W.X., Wang, X.C., Li, Q.L., Liu, Y., Tang, G.Q., Gao, Y.Y., and Wu, F.Y., 2010, SIMS U-Pb zircon geochronology of porphyry Cu-Au-(Mo) deposits in the Yangtze River Metallogenic Belt, eastern China: Magmatic response to early Cretaceous lithospheric extension: Lithos, v. 119, p. 427–438, https://doi.org/10.1016/j.lithos.2010.07.018.

Li, Y., Li, X. H., Selby, D., and Li, J. W., 2017a, Pulsed magmatic fluid release for the formation of porphyry deposits: tracing fluid evolution in absolute-time from the Tibetan Qulong Cu-Mo deposit: Geology, v. 46, no. 1, p. 7-11, https://doi:10.1130/G39504.1.

Li, Y., Li, J.W., Li, X.H., Selby, D., Huang, G.H., Chen, L.J., and Zheng, K., 2017b, An Early Cretaceous carbonate replacement origin for the Xinqiao stratabound massive sulfide deposit, Middle-Lower Yangtze Metallogenic Belt, China: Ore Geology Reviews, v. 80, p. 985–1003, https://doi.org/10.1016/j.oregeorev.2016.08.017.

Mao, J.W., Xie, G.Q., Duan, C., Pirajno, F., Ishiyama, D., and Chen, Y.C., 2011, A tectono-genetic model for porphyry-skarn-stratabound Cu-Au-Mo-Fe and magnetite-apatite deposits along the Middle-Lower Yangtze River Valley, Eastern China: Ore Geology Reviews, v. 43, p. 294–314, https://doi.org/10.1016/j.oregeorev.2011.07.010.

Meinert, L.D., 1982, Skarn, Manto, and Breccia Pipe Formation in Sedimentary-Rocks of the Cananea Mining District, Sonora, Mexico: Economic Geology and the Bulletin of the Society of Economic Geologists, v. 77, p. 919–949, https://doi.org/10.2113/gsecongeo.77.4.919.

Pan, Y.M., and Dong, P., 1999, The Lower Changjiang (Yangzi/Yangtze River) metallogenic belt, east central China: Intrusion- and wall rock-hosted Cu-Fe-Au, Mo, Zn, Pb, Ag deposits: Ore Geology Reviews, v. 15, p. 177–242, https://doi.org/10.1016/S0169-1368(99)00022-0.

Pirajno, F., and Zhou, T., 2015, Intracontinental Porphyry and Porphyry-Skarn Mineral Systems in Eastern China: Scrutiny of a Special Case "Made-in-China": Economic Geology and the Bulletin of the Society of Economic Geologists, v. 110, p. 603–629, https://doi.org/10.2113/econgeo.110.3.603.

Sato, T., 1984, Manto type copper deposits in Chile: A review: Bulletin of the Geological Survey of Japan, v. 35, p. 565–582.

Selby, D., Kelley, K.D., Hitzman, M.W., and Zieg, J., 2009, Re-Os sulfide (bornite, chalcopyrite, and pyrite) systematics of the carbonate-hosted copper deposits at Ruby Creek, southern Brooks Range, Alaska: Economic Geology and the Bulletin of the Society of Economic Geologists, v. 104, p. 437–444, https://doi.org/10.2113/gsecongeo.104.3.437.

Sillitoe, R.H., 2010, Porphyry Copper Systems: Economic Geology and the Bulletin of the Society of Economic Geologists, v. 105, p. 3–41, https://doi.org/10.2113/gsecongeo.105.1.3.

Sweeney, R. E., and Kaplan, I. R., 1973, Pyrite Framboid Formation; Laboratory Synthesis and Marine Sediments: Economic Geology, v. 68, no. 5, p. 618-634. https://doi.org/10.2113/gsecongeo.68.5.618

Stein, H.J., 2014, Dating and Tracing the History of Ore Formation, *in* Turekian, H. D. H. K., ed., Treatise on Geochemistry (Second Edition): Oxford, Elsevier, p. 87–118, https://doi.org/10.1016/B978-0-08-095975-7.01104-9.

Wang, G.-G., and Ni, P., 2009, Fluid inclusions study for the pyrite vein beneath Xinqiao stritiform massive Cu deposit [in Chinese]: Acta Mineralogica Sinica, v. 29, p. 256.

Xie, Q.-Q., Chen, T.-H., Fan, Z.-L., Xu, X.-C., Zhou, Y.-F., Shi, W.-B., and Xue, J.-J., 2014, Morphological characteristics and genesis of colloform pyrite in Xinqiao Fe-S deposit, Tongling, Anhui Province [in Chinese]: Scientia Sinica Terrae, v. 44, p. 2665–2674.

Xu, G., and Zhou, J., 2001, The Xinqiao Cu-S-Fe-Au deposit in the Tongling mineral district, China: Synorogenic remobilization of a stratiform sulfide deposit: Ore Geology Reviews, v. 18, p. 77–94, https://doi.org/10.1016/S0169-1368(01)00017-8.

Yang, G., Chen, J.F., Du, A.D., Qu, W.J., and Yu, G., 2004, Re-Os dating of the Mo-bearing black shale from Laoyalong, Anhui [in Chinese]: Chinese Science Bulletin, v. 49, p. 1205–1208.

Zeng, P.-S., Pei, R.-F., and Hou, Z.-Q., 2002, Sedex-type massive sulfide deposits in Tongling Block, Anhui [in Chinese]: Mineralium Deposita, v. 21, p. 532–535.

Zhang, Y., Shao, Y.J., Li, H.B., and Liu, Z.F., 2017, Genesis of the Xinqiao Cu-S-Fe-Au deposit in the Middle-Lower Yangtze River Valley metallogenic belt, Eastern China: Constraints from U-Pb-Hf, Rb-Sr, S, and Pb isotopes: Ore Geology Reviews, v. 86, p. 100–116, https://doi.org/10.1016/j.oregeorev.2017.02.014.

Zhou, T.F., Yu, F., and Yuan, F., 2008, Advances on petrogensis and metallogeny study of the mineralization belt of the Middle and Lower Reaches of the Yangtze River area [in Chinese with English abstract]: Yanshi Xuebao, v. 24, p. 1665–1678.

FIGURE CAPTIONS

Figure 1. A), Distribution of porphyry-skarn and stratabound deposits in the Middle–Lower Yangtze River metallogenic belt and their spatial association with Early Cretaceous granites. Modified after Pan and Dong (1999) and Mao et al. (2011). B), Geological map of the Xinqiao stratabound ore deposit. C), Cross section of the Xinqiao deposit and relevant chronological data. 1, Li et al. (2017b); 2, Yang et al. (2004); 3, this study; 4, Guo et al. (2011); 5, Zhang et al. (2017).

Figure 2. Representative pyrite mineralization at Xinqiao and their Re–Os ages. A), Euhedral pyrite grains (py1) cemented by calcite from the stratabound ore body. B), Colloform pyrite (py2) from the stratabound ore body, which is composed of fine-grained (80 nm–1.5 μm) cubic pyrite grains, with local distribution of calcite grains. No framboidal pyrite grains are observed in this study. C), Pyrite samples (py3) from the garnet-bearing skarn ore. D), Pyrite samples (py4) hosted by sandstone beneath the stratabound ore body. E), Re–Os isochrons of py1, py2 and py3. F), Model ages of py4 and their correlation with Re abundances. Also shown are data from Guo et al. (2011). Py = pyrite, cal = calcite, qtz = quartz, gar = garnet. Resin refers to the materials used for

making mounts. MSWD = Mean Squared Weighted Deviation. All uncertainties are at the 2-sigma level.

Figure 3. Trace element compositions of the studied pyrite samples. A), Py2 is characterized by high total abundances of Co, Ni, Ag, Au, Tl, Ba; py4 is enriched in Cu, W, Pb, Zn. In contrast, py1 and py3 are depleted in these trace elements. B), The model ages of py4 are positively correlated with their total abundances of Co, Ni, Ag, Au, Tl and Ba. Uncertainties are smaller than the symbol size.

Figure 4. Sketch illustrating the genesis of intrusion-related stratabound deposits in the Middle–Lower Yangtze metallogenic belt, which is temporally and spatially associated with Early Cretaceous granites, porphyry and skarn deposits. The model highlights the importance of recycling metals from metalliferous sedimentary rocks and pre-existing mineralization in the formation of intrusion-related stratabound deposits.

1GSA Data Repository item 2018xxx, Deposit geology, samples, analytical methods, Pyrite Re-Os and trace elements data, is available online at http://www.geosociety.org/datarepository/2018/ or on request from editing@geosociety.org.

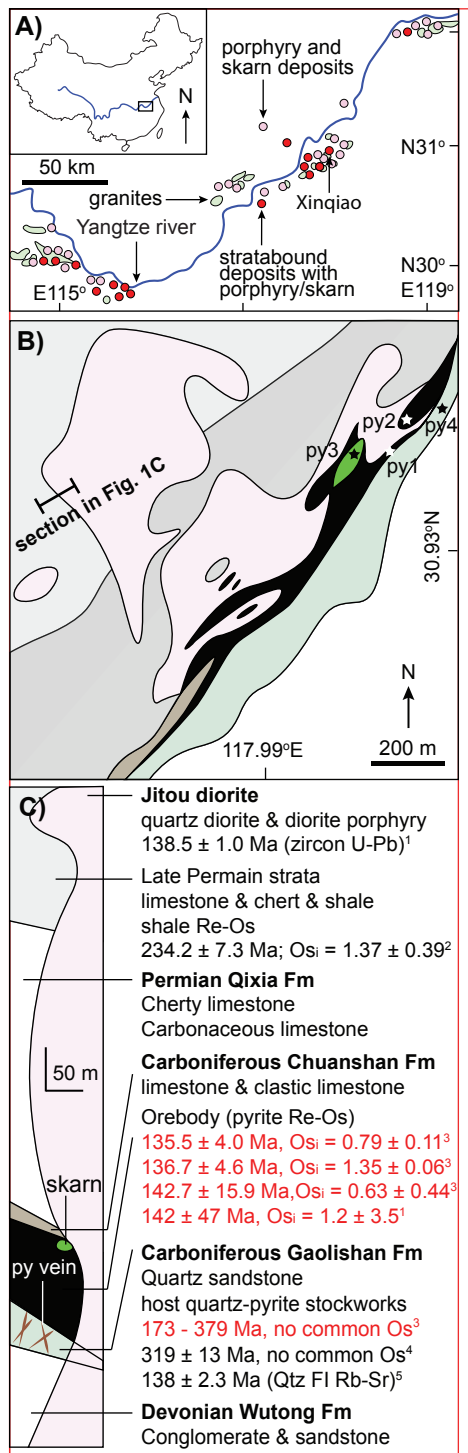
A)
N
50 km
porphyry and
skarn deposits
granites
Yangtze river
Xinqiao
stratabound
deposits with
porphyry/skarn
N31°
N30°
E115°
E119°
B)
py1
py2
py3
py4
section in Fig. 1C
30.93°N
N
117.99°E
200 m
C)
Jitou diorite
quartz diorite & diorite porphyry
138.5 ± 1.0 Ma (zircon U-Pb)[1]
Late Permain strata
limestone & chert & shale
shale Re-Os
234.2 ± 7.3 Ma; Osi = 1.37 ± 0.39[2]
Permian Qixia Fm
Cherty limestone
Carbonaceous limestone
50 m
Carboniferous Chuanshan Fm
limestone & clastic limestone
Orebody (pyrite Re-Os)
135.5 ± 4.0 Ma, Osi = 0.79 ± 0.11[3]
136.7 ± 4.6 Ma, Osi = 1.35 ± 0.06[3]
142.7 ± 15.9 Ma,Osi = 0.63 ± 0.44[3]
142 ± 47 Ma, Osi = 1.2 ± 3.5[1]
skarn
py vein
Carboniferous Gaolishan Fm
Quartz sandstone
host quartz-pyrite stockworks
173 - 379 Ma, no common Os[3]
319 ± 13 Ma, no common Os[4]
138 ± 2.3 Ma (Qtz Fl Rb-Sr)[5]
Devonian Wutong Fm
Conglomerate & sandstone

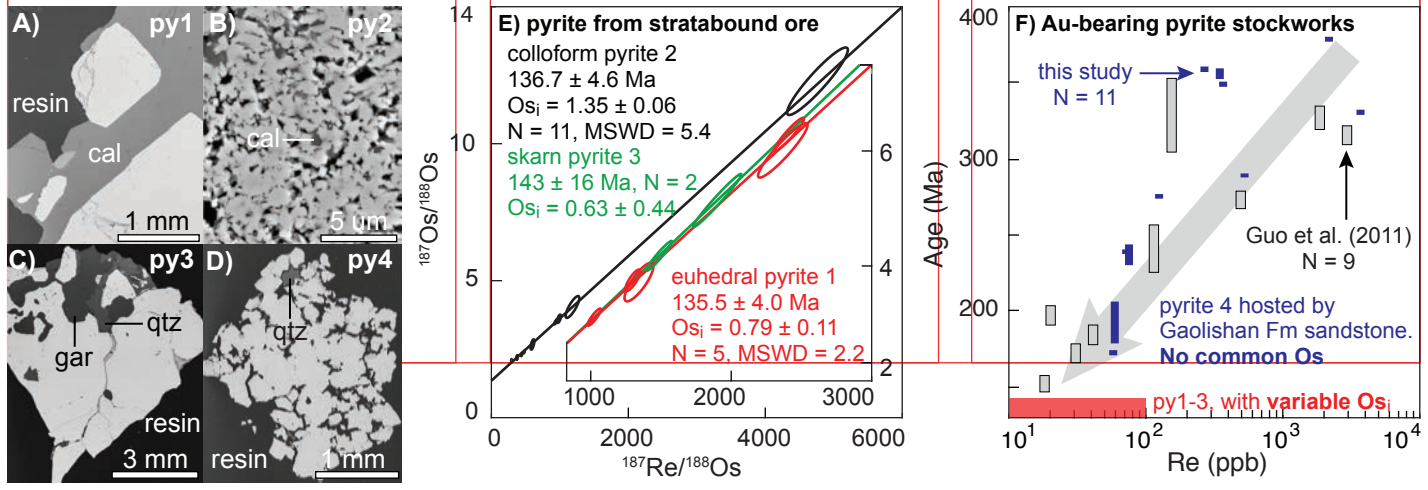
A)
py1
resin
cal
1 mm
B)
py2
cal
5 um
C)
py3
qtz
gar
resin
3 mm
D)
py4
qtz
resin
1 mm
E) pyrite from stratabound ore
colloform pyrite 2
136.7 ± 4.6 Ma
Osi = 1.35 ± 0.06
N = 11, MSWD = 5.4
skarn pyrite 3
143 ± 16 Ma, N = 2
Osi = 0.63 ± 0.44
euhedral pyrite 1
135.5 ± 4.0 Ma
Osi = 0.79 ± 0.11
N = 5, MSWD = 2.2
187Os/188Os
187Re/188Os
F) Au-bearing pyrite stockworks
this study
N = 11
Guo et al. (2011)
N = 9
pyrite 4 hosted by
Gaolishan Fm sandstone.
No common Os
py1-3, with variable Osi
Age (Ma)
Re (ppb)

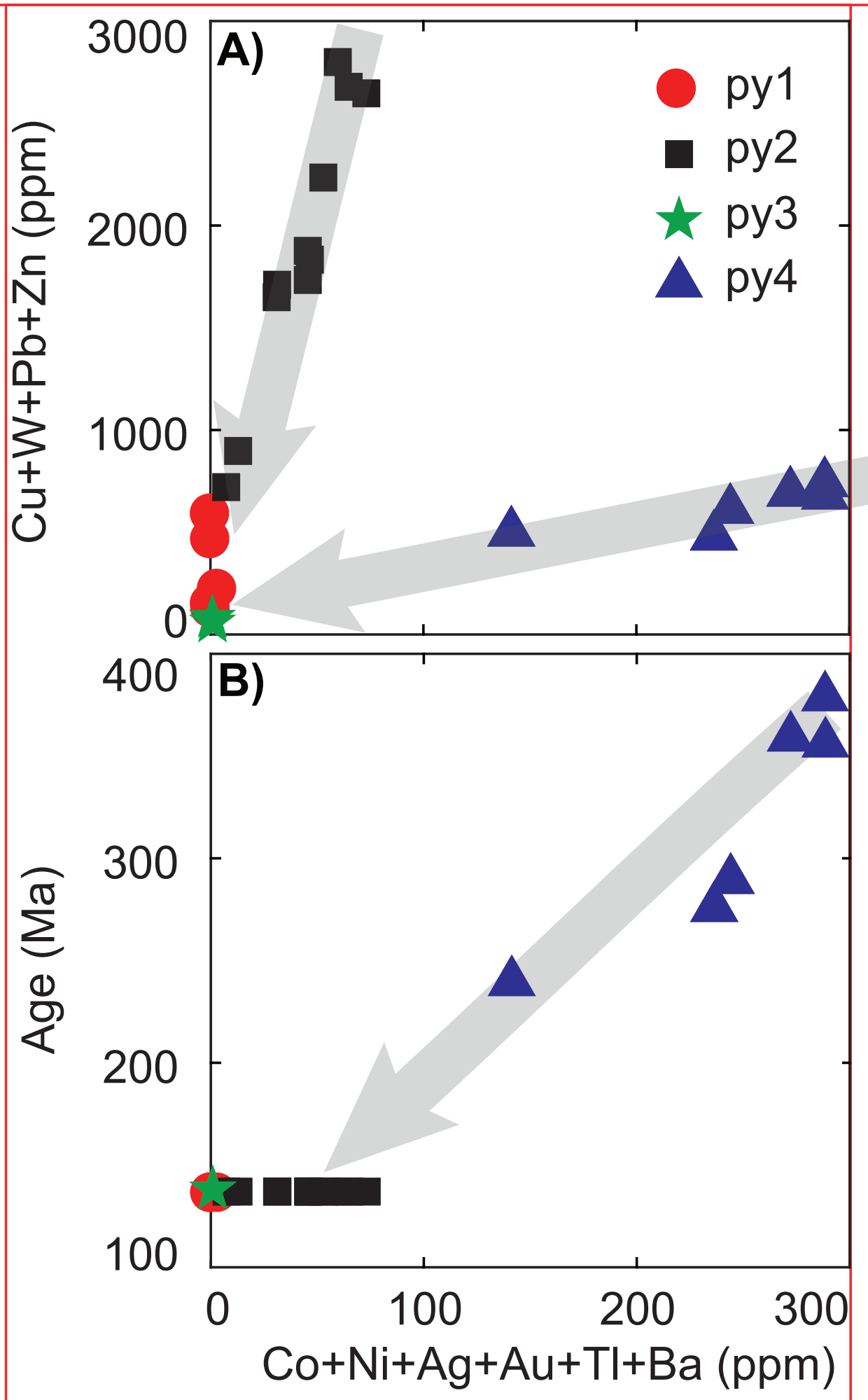
A)
B)
py1
py2
py3
py4
Cu+W+Pb+Zn (ppm)
Age (Ma)
Co+Ni+Ag+Au+Tl+Ba (ppm)
3000
2000
1000
0
400
300
200
100
0
100
200
300

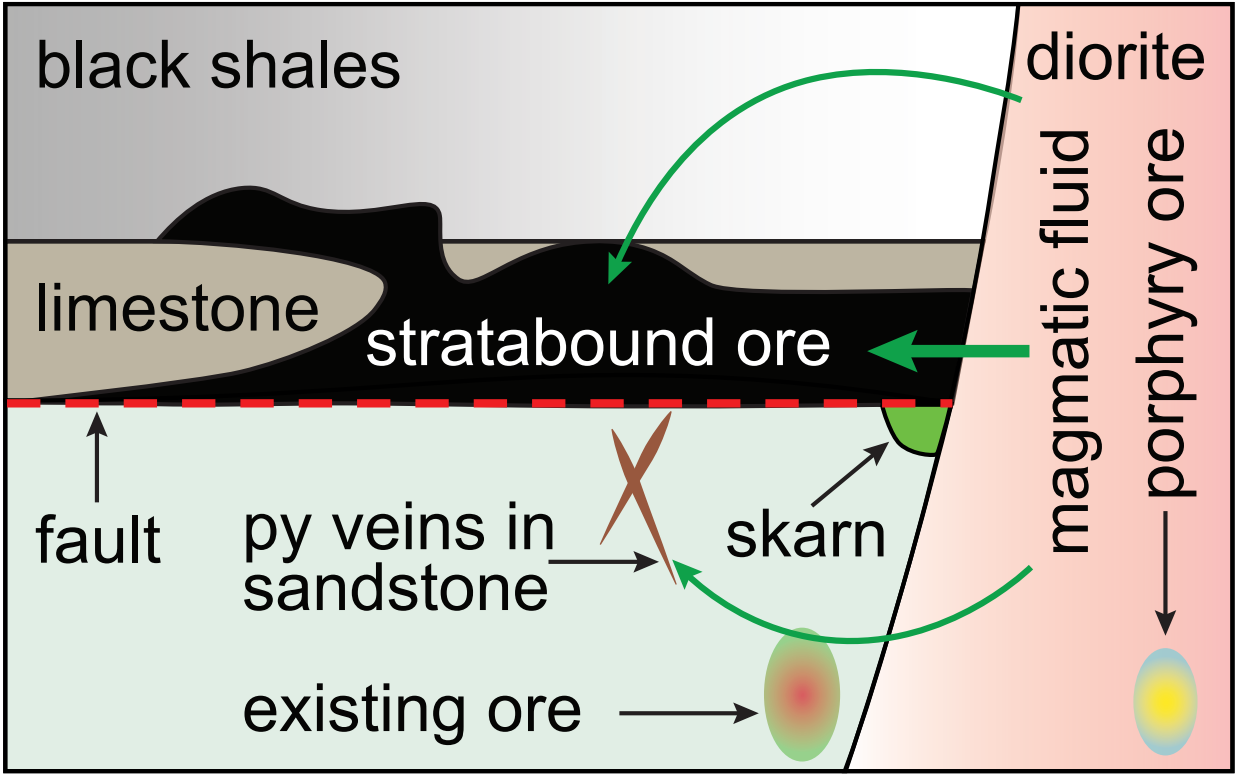
black shales
diorite
limestone
stratabound ore
magmatic fluid
porphyry ore
fault
py veins in sandstone
skarn
existing ore

Data Repository for

Multisourced metals enriched by magmatic-hydrothermal fluid in stratabound deposits of the Middle-Lower Yangtze River metallogenic belt, China

Yang Li[1,2,3*], David Selby[1,4], Xian-Hua Li[2], and Chris J. Ottley[1]

[1]*Department of Earth Sciences, Durham University, DH1 3LE Durham, UK*

[2]*State Key Laboratory of Lithospheric Evolution, Institute of Geology and Geophysics, Chinese Academy of Sciences, 10029 Beijing, China*

[3]*Department of Geology and Geophysics, Yale University, New Haven, Connecticut 06511, CT, USA*

[4]*State Key Laboratory of Geological Processes and Mineral Resources, School of Earth Resources, China University of Geosciences, Wuhan, 430074, Hubei, China*

*E-mail: yang.li@yale.edu; cugliyang@126.com

A1. Deposit Geology, Sample location and details

At the Xinqiao deposit, the stratabound ore body (Fig. DR1) strikes NE-SW and dips (~45°) northwest, with horizontal and vertical extensions and an average thickness of 2550 m, 1810 m, and 21 m, respectively (Xu and Zhou, 2001). The stratabound ore body (Fig. DR2A) predominantly comprises Cu-bearing massive euhedral pyrite (py1, Figure 2A and DR2B) and colloform pyrite (py2, Figure 2B and DR2C), although massive chalcopyrite and anhedral pyrite are also present. The Jitou diorite (SIMS U-Pb zircon age of ~138.5 ± 1.0 Ma; Li et al., 2017) was emplaced into the Carboniferous-Permian carbonate units, which is associated with intense skarn garnet-diopside-epidote alteration (Zhang et al., 2017), that is crosscut by ~1 cm wide pyrite ± chalcopyrite veins (py3, Figures 2C and DR2D). Beneath the stratabound ore body, the Gaolishan Formation sandstone is extensively fractured (Fig. DR2E), and hosts vertical to sub-vertical Au-bearing pyrite stockworks (py4, Fig. 2D) with ~1 – 10 cm wide silicified and sericite-bearing selvages (Guo et al., 2011).

Sample locations are illustrated in Figure 1B and Figure DR3. In Figure DR3, the portion that has been removed/mined is the stratabound ore body. All samples were collected from the outcrops in the open pit. Euhedral pyrite (XQ15-9, py1) and colloform pyrite (XQ15-4, py2) samples of the stratabound orebody were collected from fresh outcrop (Fig. DR1, DR1A) exposed during the mining process. The outcrop is located in the southwest wall of the open pit, where the colloform pyrite ore and euhedral pyrite ore have a sharp contact relationship (Fig. DR2A). No direct relationship between the stratabound ore and country rocks was observed at Xinqiao. The colloform pyrite (py2) also contains carbonate veins (<1mm – 1cm, Figs. 2B, DR2A and DR2C), but according to the sharp contact relationship between py1 and py2, a recrystallization origin of py1 from py2 is unlikely.

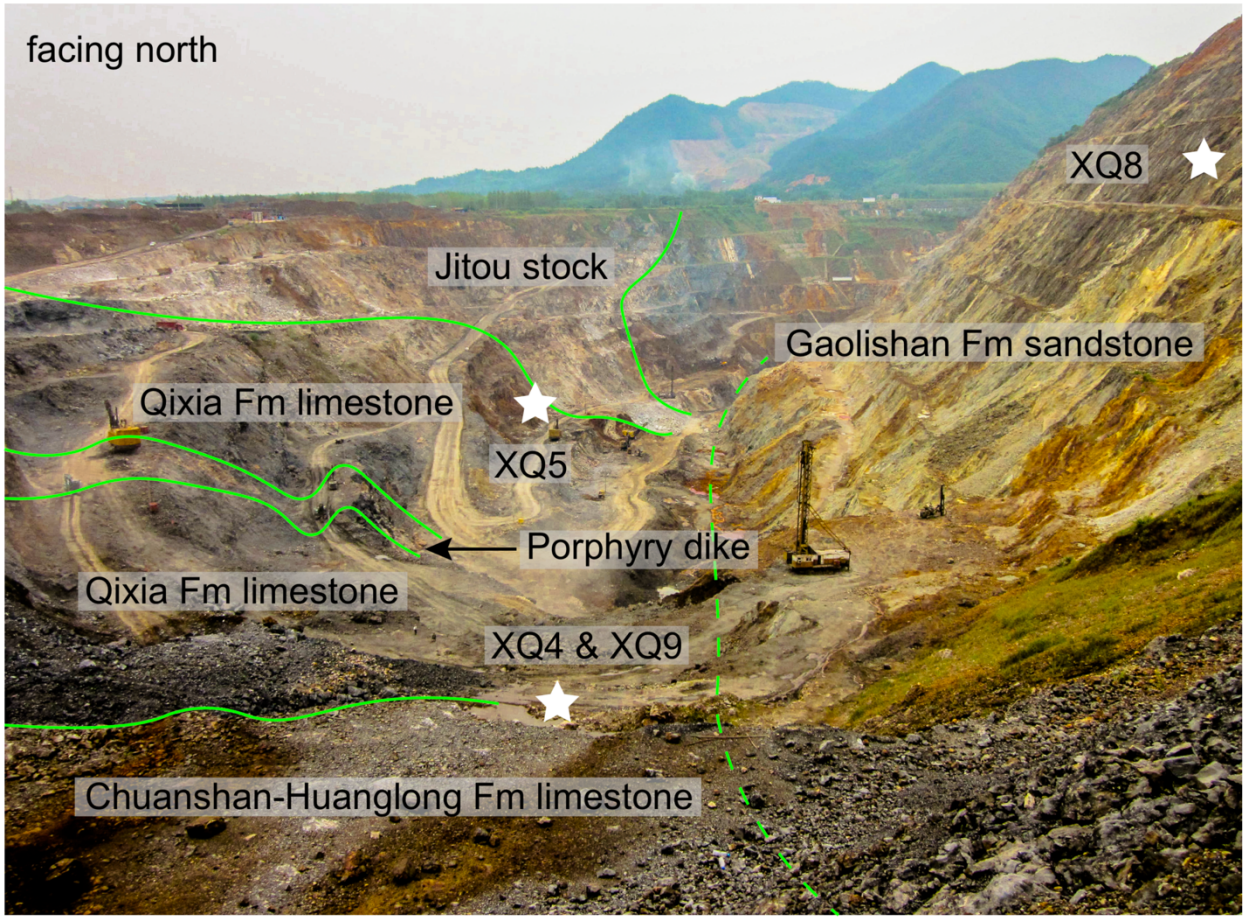

Figure DR1. A photo image of the open pit of Xinqiao, with highlighted deposit geology and sample locations.

The euhedral pyrite ore predominately comprises euhedral to sub-euhedral pyrite (<0.5 to several cm in size, Fig. 2A, DR2B) with a volume percentage of ~80%, the cements are calcite (15%) and quartz (<5%). Pyrite veins (XQ15-5, py3) hosted by the garnet-bearing skarn ore was collected from the northwest wall of the open pit where the Jitou stock intrudes limestone of Permian Qixia Formation (Fig. DR1). The sample predominately contains brown-red garnet grains (<1 cm in size), and is crosscut by pyrite veins, which in turn have been crosscut by quartz veins (Fig. 2C, DR2D). The skarn-pyrite vein (~0.5 cm width) contains sub-euhedral pyrite grains (<1 cm in size). Pyrite veins (XQ15-8, py4) beneath the stratabound orebody were collected from the southeast wall of the open pit (Fig. DR1). The veins are of variable width (<1 cm and >15 cm) and are hosted by sandstone of Carboniferous Gaolishan Formation (Fig. DR2E). The sandstone is

intensively fractured, and extensively silicified. The pyrite grains generally are euhedral, with grain sizes of 0.2 cm to 1 cm, and show open space filling features (Fig. 2D, DR2F). With the exception of silicification and sericitization, no other alteration type is observed or is documented.

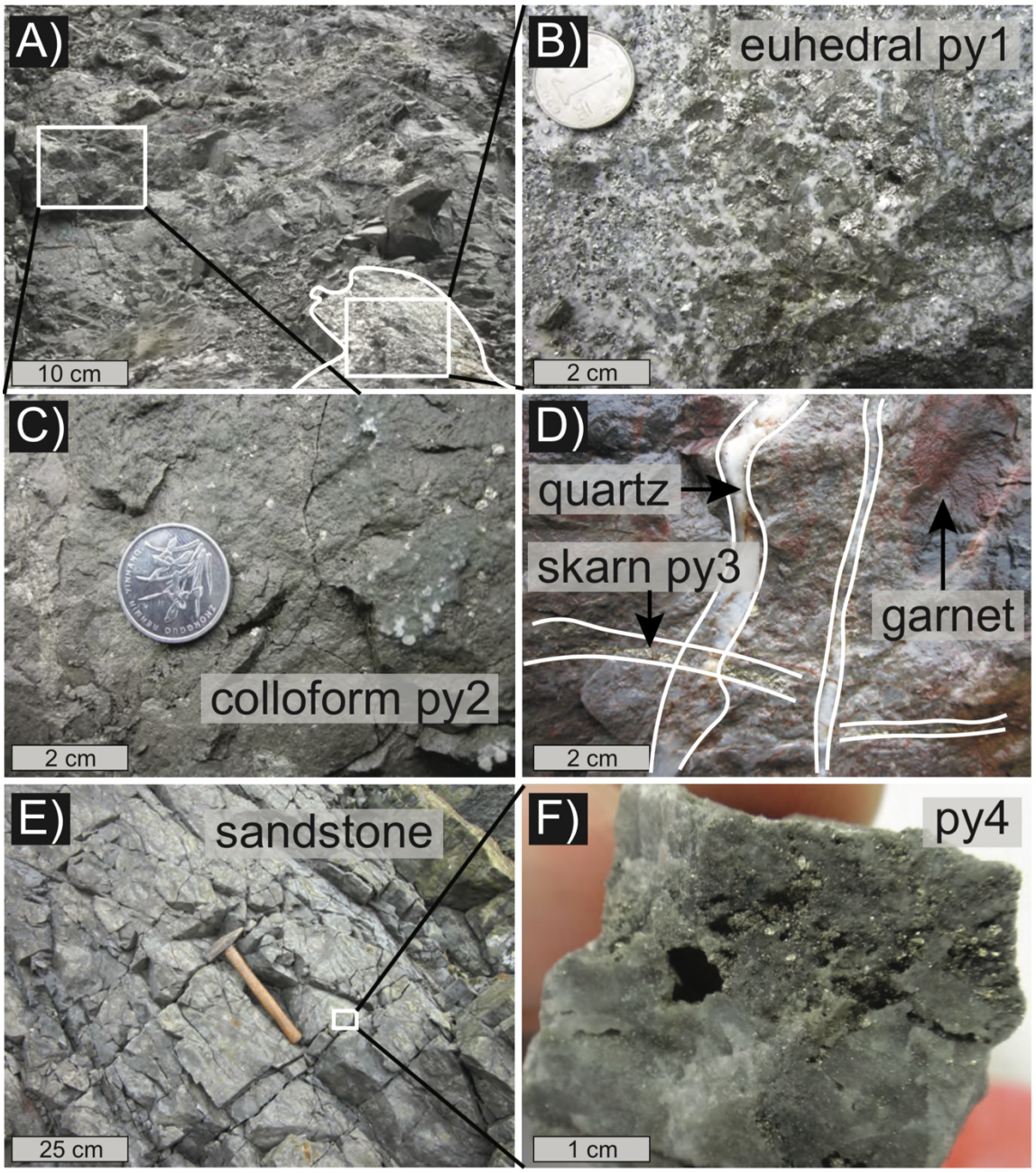

Figure DR2. Samples utilized in this study. A), The sharp contact relationship between the colloform pyrite and euhedral pyrite ores from the stratabound orebody; B), Euhedral pyrite ore (py1); C), Colloform pyrite ore (py2); D), Garnet bearing skarn ore crosscut by quartz and pyrite veins (py3); E), Pyrite veins hosted by Gaolishan Formation sandstone; F), Pyrite-quartz veins (py4) hosted by sandstone show open space filling features.

In most cases, no direct contact relationship is documented/observed between the colloform ore and sedimentary rocks, but colloform pyrite veins cross cuts the Permian limestone are observed locally (Fig. DR3). Beneath the stratabound ore bodies are vertical to sub-vertical Au-bearing pyrite stockworks hosted by the Early Carboniferous Gaolishan Formation sandstone (Guo et al., 2011; Zhang et al., 2017).

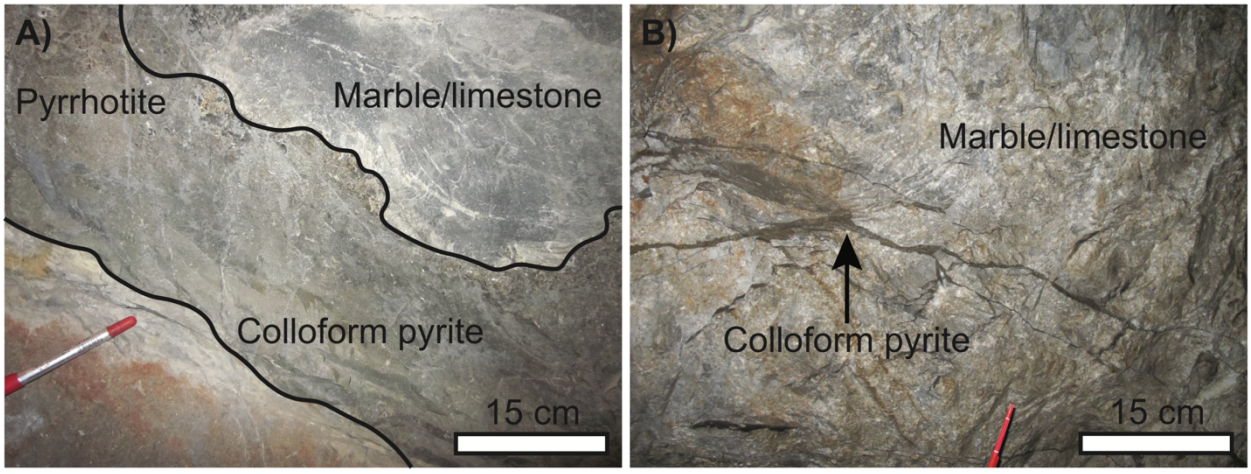

Figure DR3. Colloform pyrite ores cross-cutting Permian marble/limestone at the Dongguashan deposit (A) and the Wushan deposit (B).

A2. Pyrite Re-Os isotope analytical method

After petrographic examination, pyrite-bearing samples were crushed to 20-30 mesh and handpicked under a microscope; estimated pyrite purity is better than 98 %. The purified pyrite samples were mounted in epoxy resin for further petrographic examination (Fig. 2A) with an aim to document the texture and association with alteration assemblages. The pyrite Re-Os analytical method utilized is the same as previously documented (Selby et al., 2009; Li, et al., 2017) and is briefly outlined here. Purified pyrite aliquots were accurately weighted and loaded into a Carius tube with known amounts of a mixed Re-Os tracer solution containing ^{185}Re and ^{190}Os. The bottom part of the Carius tube was frozen in a mixture of ethanol and dry ice, and 11.5 N HCl (3 ml) and 15.5 N HNO_3 (8 ml) were added. The Carius tube was sealed from the top by a hydrogen-oxygen

torch and then kept in a steel jacket. Sample digestion and sample-spike equilibrium was achieved in an oven at 220 ^{o}C for 48 hours. Once cooled, the outside of the Carius tube was rinsed with MQ. The bottom part was frozen again in ethanol-dry ice slurry before being opened from the top by a hydrogen-oxygen torch. Osmium was isolated from the acidic digestion medium using solvent ($CHCl_3$*3 times) extraction, and then was back extracted by HBr, and finally purified through microdistillation. Rhenium was separated by solvent extraction (NaOH-acetone) from the acidic medium and then was further purified via anion exchange chromatography. The purified Re and Os were loaded onto Ni and Pt filaments, respectively, and the isotopic measurements were conducted using negative thermal ionization mass spectrometry on a Thermo Electron$^{@}$ TRITON mass spectrometer (Creaser et al. 1991; Völkening et al. 1991) at Durham University. The Os data was collected via a secondary electron multiplier in peak-hopping mode, and Re data was collected with static Faraday collectors. Total procedural blanks were monitored over the course of study. Blanks for Re and Os were 2.6 ± 0.4 and 1.5 ± 1.6 pg, respectively, with an average $^{187}Os/^{188}Os$ value of 0.21 ± 0.10 (2σ, n = 5). For the samples of this study, the presented uncertainties are fully propagated to include uncertainties in Re and Os isotopic compositions measurements, blank abundances and isotopic compositions, spike calibrations and the reproducibility of Re and Os standards. The Re-Os isochron graphs were plotted using Isoplot v4.15 program (Ludwig 2003), with the ^{187}Re decay constant of ^{187}Re of 1.666 x 10 $^{-11}a^{-1}$ (Shirey and Walker 1998; Selby et al. 2007). For pyrite samples hosted by sandstone of Gaolishan Formation, given the extremely low to absence of common Os detected, in addition to using the ^{185}Re + ^{190}Os enriched spike, we also run duplicated analyses using an ^{185}Re + normal Os spike as used for molybdenite analysis (Selby and Creaser 2001; Li et al. 2017b). For the same sample, the two methods yield similar data, however, they do not overlap within analytical uncertainty (Table DR1). This indicates that Re-Os

systematics of py4 are not homogeneous, as further supported by their element budgets (Table DR2). Nevertheless, the Re abundances and model dates of py4 from both analytical methods fall on the same trend (Fig. 2F, see main text discussion).

A3. Re-Os data and initial $^{187}Os/^{188}Os$ values

For py1, py2 and py3, their initial $^{187}Os/^{188}Os$ values are determined through isochron regression of the $^{187}Re/^{188}Os$ and $^{187}Os/^{188}Os$ data (Fig. 2B), and also recalculated at 138.5 Ma in Table DR1. The two approaches yield indistinguishable results within uncertainties. For py4, the $^{187}Re/^{188}Os$ and $^{187}Os/^{188}Os$ values are highly radiogenic (70930-170383 and 265-943; Table DR1) and imply that the bulk of the Os is ^{187}Os. The Re-Os isotope data of py4 do not yield any meaningful Re-Os isotopic data and thus their initial $^{187}Os/^{188}Os$ value is not known. In this case, an initial $^{187}Os/^{188}Os$ value must be assumed in order to calculate the best estimate for the percentage of radiogenic Os, and thus to yield an accurate and precise Re-Os model age. For the py4 sample set, owning to their exceptionally high rhenium abundances and high percentage of radiogenic Os, the overall accuracy of the percentage of radiogenic ^{187}Os (>99.55%), and hence the model age, is relatively insensitive to the assumed initial $^{187}Os/^{188}Os$ values (Table DR2).

In order to put tight constraints on the genesis of py4, we further investigate the two proposed genetic scenarios as follows. If we consider py4 are Carboniferous in age (i.e., 320 Ma), then the initial $^{187}Os/^{188}Os$ values of these samples would need to be highly variable (-223 and 59), but the presence of both positive and negative values is a geological unlikely scenario. A Cretaceous age (i.e., 138.5 Ma) would also require the sample set to possess highly variable initial $^{187}Os/^{188}Os$ values (54 to 549). But the initial $^{187}Os/^{188}Os$ values are geologically possible, which could be generated through the interaction with ^{187}Os-rich phases (e.g., molybdenite; see main text for discussion). Such a hypothesis is further supported by the correlation between the Re-Os model

ages, rhenium abundances and Co + Ni + Ag + Ba + Au + Tl values (Figs. 2F and 3C; see main text for discussion), suggesting that a higher degree of interaction with Re- and ^{187}Os-rich phases resulted in the inheritance of more Re, ^{187}Os and trace elements. To summarize, we consider a Carboniferous age is unlikely for py4, and instead propose that a Cretaceous age is the most plausible scenario, which is in accordance with the Re-Os age constrains of py1, py2, py3 and geological observations.

A4. Pyrite trace element analytical method

Trace-element abundances were determined using a modification of the procedure of Ottley et al., (2003). Pyrite grains (~100 mg) were digested in 6ml inverse aqua-regia (2:1 mix of 15.5N HNO_3 and 11.5N HCl) in Teflon beakers at 220 °C for 24 h and then evaporated to dryness at 80 °C. At this stage, 1 ml 16N HNO_3 was added and evaporated to near dryness. This process was repeated for three times, and followed by the addition of 10 ml 4N HNO_3. The sample was capped and heated overnight at 100 °C. Once cooled, the solution was transferred to a 50ml centrifuge tube and brought up to 50 ml MQ H_2O. A 1:10 dilution of the sample solution was made prior to sample analysis. Trace elements were analyzed using the Thermo$^{@}$ XSERIES 2 mass spectrometer at Durham University. In-house and international reference materials (W-2, BHVO-1, AGV1) were used for calibration and multiple blank analysis were included for each sample set. Reproducibility of elemental runs is estimated to be better than 5% (2 SD).

A5. List of tables and figures

Table DR1. Synopsis of the Pyrite Re-Os data from the Xinqiao deposit.

Table DR2. Synopsis of the pyrite trace element data from the Xinqiao deposit.

Figure DR3. Colloform pyrite ores intruded into Permian marble/limestone at Dongguashan deposit (A) and Wushan deposit (B).

Figure DR2. A photo image of the open pit of Xinqiao, with highlighted deposit geology and sample locations.

Figure DR2. Samples utilized in this study. A), The sharp contact relationship between the colloform pyrite and euhedral pyrite ores from the stratabound orebody; B), Euhedral pyrite ore (py1); C), Colloform pyrite ore (py2); D), Garnet bearing skarn ore crosscut by quartz and pyrite veins (py3); E), Pyrite veins hosted by Gaolishan Formation sandstone; F), Pyrite-quartz veins (py4) hosted by sandstone show open space filling features.

References

Creaser RA, Papanastassiou DA, Wasserburg GJ (1991) Negative Thermal Ion Mass-Spectrometry of Osmium, Rhenium, and Iridium. Geochim Cosmochim Acta 55:397–401. doi: Doi 10.1016/0016-7037(91)90427-7

Guo, W.M., Lu, J.J., Jiang, S.Y., Zhang, R.Q., and Qi, L., 2011, Re-Os isotope dating of pyrite from the footwall mineralization zone of the Xinqiao deposit, Tongling, Anhui Province: Geochronological evidence for submarine exhalative sedimentation: Chinese Science Bulletin, v. 56, p. 3860–3865, https://doi.org/10.1007/s11434-011-4770-y.

Li Y, Li JW, Li XH, et al (2017a) An Early Cretaceous carbonate replacement origin for the Xinqiao stratabound massive sulfide deposit, Middle-Lower Yangtze Metallogenic Belt, China. Ore Geol Rev 80:985–1003. doi: 10.1016/j.oregeorev.2016.08.017

Li Y, Selby D, Condon D, Tapster S (2017b) Cyclic magmatic-hydrothermal evolution in porphyry systems: High-precision U-Pb and Re-Os geochronology constraints from the Tibetan Qulong porphyry Cu-Mo deposit. Econ Geol 112:1419–1440. doi: 10.5382/econgeo.2017.4515

Ludwig KR (2003) User's manual for Isoplot 3.00: a geochronological toolkit for Microsoft Excel. Kenneth R. Ludwig

Ottley CJ, Pearson DG, Irvine GJ (2003) A Routine Method for the Dissolution of Geological Samples for the Analyses of REE and Trace Elements Via ICP-MS. Plasma Source Mass Spectrom Appl Emerg Technol 221–230. doi: 10.1039/9781847551689-00221

Selby D, Creaser RA (2001) Re-Os geochronology and systematics in molybdenite from the Endako porphyry molybdenum deposit, British Columbia, Canada. Econ Geol 96:197–204. doi: Doi 10.2113/96.1.197

Selby D, Creaser RA, Stein HJ, et al (2007) Assessment of the 187Re decay constant by cross calibration of Re–Os molybdenite and U–Pb zircon chronometers in magmatic ore systems. Geochim Cosmochim Acta 71:1999–2013. doi: 10.1016/j.gca.2007.01.008

Selby D, Kelley KD, Hitzman MW, Zieg J (2009) Re-Os sulfide (bornite, chalcopyrite, and pyrite) systematics of the carbonate-hosted copper deposits at Ruby Creek, Southern Brooks Range, Alaska. Econ Geol 104:437–444.

Shirey SB, Walker RJ (1998) The Re-Os isotope system in cosmochemistry and high-temperature geochemistry. Annu Rev Earth Planet Sci 26:423–500. doi: DOI 10.1146/annurev.earth.26.1.423

Völkening J, Walczyk T, Heumann KG (1991) Osmium isotope ratio determinations by negative thermal ionization mass spectrometry. Int J Mass Spectrom Ion Process 105:147–159.

Xu, G., and Zhou, J., 2001, The Xinqiao Cu-S-Fe-Au deposit in the Tongling mineral district, China: Synorogenic remobilization of a stratiform sulfide deposit: Ore Geology Reviews, v. 18, p. 77–94, https://doi.org/10.1016/S0169-1368(01)00017-8.

Zhang, Y., Shao, Y.J., Li, H.B., and Liu, Z.F., 2017, Genesis of the Xinqiao Cu-S-Fe-Au deposit in the Middle-Lower Yangtze River Valley metallogenic belt, Eastern China: Constraints from U-Pb-Hf, Rb-Sr, S, and Pb isotopes: Ore Geology Reviews, v. 86, p. 100–116, https://doi.org/10.1016/j.oregeorev.2017.02.014.

Table DR1, Pyrite Re-Os data from Xinqiao deposit

Sample	Weight (g)	Re (ppb)	2σ	Os (ppt)	2σ	^{192}Os (ppt)	2σ	^{187}Re/^{188}Os	2σ	^{187}Os/^{188}Os	2σ	rho	%^{187}Osr	Os*i* @ *138.5 Ma*	2σ
Py1, euhedral pyrite from stratabound orebody															
XQ15-9-1	0.42	1.47	0.01	7.76	0.24	2.18	0.13	1343.42	82.83	3.72	0.27	0.820	76.6	*0.63*	*0.46*
XQ15-9-2	0.41	2.58	0.02	14.11	0.27	3.95	0.13	1299.34	42.92	3.75	0.15	0.823	76.8	*0.76*	*0.24*
XQ15-9-4	0.43	2.03	0.01	7.32	0.21	1.71	0.10	2367.32	141.74	6.01	0.38	0.929	85.5	*0.56*	*0.71*
XQ15-9-5	0.40	1.58	0.02	10.29	0.19	3.06	0.11	1024.68	38.02	3.11	0.12	0.891	72.0	*0.75*	*0.21*
XQ15-9-6	0.41	3.59	0.02	12.94	0.25	2.96	0.10	2412.85	84.13	6.29	0.23	0.940	86.2	*0.73*	*0.42*
													weighted mean	***0.73***	***0.14***
Py2, colloform pyrite from stratabound orebody															
XQ15(coarse)-4-1	0.40	9.28	0.03	68.95	0.74	19.81	0.21	932.11	10.26	3.47	0.05	0.649	65.5	*1.33*	*0.08*
XQ15(coarse)-4-2	0.41	5.62	0.02	116.49	0.95	38.25	0.35	292.47	2.88	2.10	0.03	0.670	42.9	*1.43*	*0.03*
XQ15(coarse)-4-3	0.45	2.44	0.01	26.12	0.61	8.09	0.29	599.77	21.53	2.67	0.15	0.614	55.1	*1.29*	*0.20*
XQ15(coarse)-4-4	0.41	3.22	0.02	45.09	0.55	14.48	0.24	442.86	7.64	2.31	0.05	0.687	48.1	*1.29*	*0.07*
XQ15(coarse)-4-5	0.45	6.89	0.02	18.02	0.66	2.88	0.23	4762.58	356.88	12.28	0.99	0.928	90.2	*1.32*	*1.81*
XQ15(fine)-4-0	0.40	1.20	0.02	7.37	0.25	2.01	0.14	1184.49	80.40	4.04	0.32	0.819	70.3	*1.32*	*0.51*
XQ15(fine)-4-1	0.40	7.64	0.02	56.07	0.62	16.05	0.20	947.50	12.09	3.52	0.06	0.729	65.9	*1.34*	*0.09*
XQ15(fine)-4-2	0.43	8.14	0.03	133.26	1.75	43.35	0.57	373.75	5.17	2.19	0.06	0.448	45.2	*1.33*	*0.07*
XQ15(fine)-4-3	0.40	2.22	0.02	36.16	0.49	11.76	0.17	375.33	6.10	2.20	0.06	0.441	45.4	*1.33*	*0.08*
XQ15(fine)-4-4	0.41	3.93	0.02	51.21	0.51	16.31	0.19	478.98	6.02	2.40	0.04	0.657	50.0	*1.30*	*0.05*
XQ15(fine)-4-5	0.41	5.47	0.03	38.80	0.67	11.02	0.24	987.86	21.49	3.61	0.12	0.625	66.7	*1.33*	*0.17*
													weighted mean	***1.36***	***0.02***
Py3, euhedral pyrite from garnet bearing skarn ore															
XQ15-5-3	0.41	1.55	0.02	7.66	0.42	2.07	0.31	1490.23	73.57	4.18	0.21	0.961	71.3	*0.74*	*0.27*
XQ15-5-4	0.40	1.35	0.02	5.67	0.41	1.41	0.31	1904.13	137.40	5.16	0.38	0.980	69.8	*0.77*	*0.49*
													weighted mean	**0.74**	**0.24**

Py4, euhedral pyrite from the quartz-pyrite stockworks hosted by Gaolishan Formation sandstone

Name		Re (ppb)	2σ	Os (ppt)	2σ	^{192}Os (ppt)	2σ	^{187}Re/^{188}Os	2σ	^{187}Os/^{188}Os	2σ	rho	^{187}Re (ppb)	2σ	^{187}Osr (ppt)[1]	2σ	%^{187}Osr[1]	Age	2σ	Os*i* for 138.5 Ma	Os*i* for 320 Ma
XQ15-8-1	0.10	3692.22	11.19	12902.16	230.79	43.11	0.81	170382.78	3252.10	942.81	18.42	0.953	2320.69	7.03	12825.12	66.36	99.87	330.8	1.7	549.2	32.0
XQ15-8-2	0.10	525.56	1.59	1615.55	54.30	10.54	0.78	99163.29	7351.46	480.52	35.66	0.997	330.33	1.00	1596.71	7.45	99.75	289.4	1.3	251.4	-49.5
XQ15-8-3	0.20	267.88	0.80	1020.06	32.32	6.02	0.39	88465.51	5778.02	531.51	34.78	0.996	168.37	0.50	1010.06	5.14	99.85	359.0	1.8	327.1	58.6
XQ15-8-4	0.30	124.95	0.37	367.80	12.53	3.50	0.27	70929.58	5410.18	327.72	25.03	0.997	78.54	0.23	361.54	1.91	99.63	275.7	1.5	163.9	-51.4
XQ15-8-5	0.20	366.51	1.09	1359.73	36.10	8.84	0.40	82464.29	3754.56	482.29	22.03	0.992	230.37	0.69	1343.93	6.50	99.75	349.2	1.7	291.8	41.5
XQ15-8-6	0.41	71.81	0.21	182.67	8.55	1.37	0.20	104594.60	15084.31	418.85	60.45	0.999	45.14	0.13	180.40	1.14	99.81	239.4	1.5	177.2	-140.3
XQ15-8-7	0.30	57.79	0.17	107.23	6.08	1.26	0.27	91223.10	19240.35	264.84	55.91	0.999	36.32	0.11	104.98	1.01	99.55	173.2	1.7	54.1	-222.8

1, Abundances and percentage of radiogenic 187Os are estimated with an initial ^{187}Os/^{188}Os value of 1.2, see main text and DR for discussions.

Py4, euhedral pyrite from the quartz-pyrite stockworks hosted by Gaolishan Formation sandstone, re-analysed using a spike enriched in ^{185}Re with a normal Os composition as used for molybdenite

Sample	wt	Re(ppb)	2σ	^{187}Re(ppb)	2σ	^{187}Os(ppt)	2σ	Age	2σ
XQ15-8-1	0.15	2172.54	7.32	1365.48	4.60	8641.73	23.47	378.7	1.6
XQ15-8-5	0.25	346.61	2.46	217.85	1.55	1296.32	8.85	356.1	3.5
XQ15-8-6	0.44	75.34	1.53	47.35	0.96	187.66	3.78	237.4	6.8
XQ15-8-7	0.16	59.32	2.97	37.29	1.87	120.07	6.01	193.0	13.7

Common Os cannot be detected with S/N spike.

Table DR2, Pyrite trace elements data from Xinqiao deposit

	weight/g	Mn ppm	Sb ppm	Cu ppm	Pb ppm	Zn ppm	Mo ppm	W ppm	Ag ppm	Au ppm	Ba ppm	Co ppm	Ni ppm	Tl ppm	Co+Ni+Ag+Ba+Au+Tl ppm	Cu+Zn+Mo+W+Pb ppm	Re ppb	Age Ma
Py1, euhedral pyrite from stratabound orebody																		
XQ15-9-1	0.1	2466.1	0.0	155.5	8.3	10.7	0.0	36.7	4.1	0.0	0.0	0.0	0.0	0.0	4.2	211.2	1.5	135.3
XQ15-9-2	0.1	1329.7	0.0	111.4	3.6	6.9	0.0	18.2	0.9	0.0	0.0	0.0	0.0	0.0	0.9	140.0	2.6	135.3
XQ15-9-4	0.1	2817.3	0.0	555.4	6.7	4.9	0.0	12.3	0.9	0.0	0.0	0.0	0.0	0.0	0.9	579.3	2.0	135.3
XQ15-9-5	0.1	2678.3	0.0	407.9	6.4	6.5	0.0	34.5	1.0	0.0	0.0	0.0	0.0	0.0	1.0	455.4	1.6	135.3
XQ15-9-6	0.1	2814.8	0.0	52.2	7.7	16.4	0.0	40.6	1.0	0.0	0.0	0.0	0.0	0.0	1.1	116.8	3.6	135.3
Py2, colloform pyrite from stratabound orebody																		
XQ15(fine)-4-0	0.1	5318.4	110.7	769.3	1249.6	190.0	25.7	0.0	27.3	0.0	0.0	0.0	0.0	0.0	53.0	2234.6	1.2	137.0
XQ15(fine)-4-1	0.1	498.2	137.1	648.0	1054.8	11.0	19.9	0.0	25.8	0.0	0.0	0.0	0.0	0.0	45.7	1733.7	7.6	137.0
XQ15(fine)-4-2	0.1	2299.2	193.6	981.2	1601.8	20.9	42.5	0.0	30.6	0.0	0.0	0.0	0.0	0.0	73.2	2646.5	8.1	137.0
XQ15(fine)-4-3	0.1	835.5	124.4	552.2	1077.8	5.1	14.6	0.0	16.5	0.0	0.0	0.0	0.0	0.0	31.1	1649.6	2.2	137.0
XQ15(fine)-4-4	0.1	2967.5	153.8	1549.3	1193.0	25.4	31.8	0.0	28.0	0.0	0.0	0.0	0.0	0.0	59.8	2799.5	3.9	137.0
XQ15(fine)-4-5	0.1	148.4	0.6	753.2	129.7	7.4	7.3	0.0	5.6	0.0	0.0	0.0	0.0	0.0	13.0	897.6	5.5	137.0
XQ15(coarse)-4-1	0.1	632.7	139.9	724.4	1100.6	30.8	20.2	0.0	25.5	0.0	0.0	0.0	0.0	0.0	45.7	1876.0	9.3	137.0
XQ15(coarse)-4-2	0.1	2200.9	181.0	984.2	1642.7	16.1	35.5	0.0	29.4	0.0	0.0	0.0	0.0	0.0	64.9	2678.5	5.6	137.0
XQ15(coarse)-4-3	0.1	1070.7	118.4	581.2	1107.0	6.8	15.4	0.0	15.9	0.0	0.0	0.0	0.0	0.0	31.3	1710.5	2.4	137.0
XQ15(coarse)-4-4	0.1	2045.6	140.0	748.1	1043.5	16.5	24.7	0.0	22.0	0.0	0.0	0.0	0.0	0.0	46.7	1832.8	3.2	137.0
XQ15(coarse)-4-5	0.1	139.5	0.6	555.9	159.5	4.8	0.4	0.0	7.0	0.0	0.0	0.0	0.0	0.0	7.4	720.7	6.9	137.0
Py3, euhedral pyrite from garnet bearing skarn ore																		
XQ15-5-3	0.1	1897.4	0.0	11.1	7.3	18.9	0.0	44.9	0.9	0.0	0.0	0.0	0.0	0.0	0.9	82.2	1.6	138.0
XQ15-5-4	0.1	1625.0	0.0	22.4	3.7	12.0	0.0	20.6	1.0	0.0	0.0	0.0	0.0	0.0	1.0	58.7	1.4	138.0
Py4, euhedral pyrite from the quartz-pyrite stockworks hosted by Gaolishan Formation sandstone																		
XQ15-8-1	0.1	83.5	60.3	185.8	458.2	95.8	0.0	0.0	17.1	0.3	36.4	76.2	101.0	135.9	290.7	739.8	3692.2	378.7
XQ15-8-2	0.1	42.0	43.9	155.4	422.4	31.6	0.0	0.0	16.1	0.4	81.0	76.5	79.1	67.5	244.1	609.3	525.6	289.4
XQ15-8-3	0.1	95.3	54.9	217.4	414.2	61.9	0.0	0.0	27.9	0.1	12.2	35.1	68.2	164.0	272.3	693.5	267.9	359.0
XQ15-8-4	0.1	37.6	13.8	281.8	182.5	14.3	0.0	0.0	5.8	0.6	28.3	203.5	193.2	8.5	236.4	478.7	125.0	275.7
XQ15-8-5	0.1	73.3	44.3	209.4	396.0	74.2	0.0	0.0	22.8	0.1	69.4	63.6	96.2	102.4	290.9	679.7	366.5	356.1
XQ15-8-6	0.1	18.6	17.7	230.1	233.6	34.6	0.0	0.0	5.1	0.3	7.9	62.6	93.8	34.2	141.3	498.3	71.8	239.4